Abstract

Topography affects the amount and spatial distribution of precipitation due to orographic lift mechanisms and, in turn, influences the prevailing climate and vegetation distribution. Previous studies have predominantly focused on orographic precipitation on landform evolution for mountain chains alongside oceans. However, research on the effect of changes in precipitation regimes induced by elevation gradients (particularly in aspect-controlled semi-arid ecosystems) and its consequences for coevolving vegetation and landform patterns are limited. In this study, the Channel-Hillslope Integrated Landscape Development (CHILD) landscape evolution model (LEM) coupled with the vegetation dynamics Bucket Grassland Model (BGM) was used to analyse the coevolution of semi-arid landform-vegetation ecosystems. The CHILD+BGM model was run under different combinations of precipitation and solar radiation settings. The three precipitation settings considered were uniform, elevation control, and orographic control precipitation; while the two radiation settings used were spatially uniform and spatially varied radiation. Based on these different precipitation and solar radiation settings, drainage network, aspect, and elevation control were identified as the major drivers of the distribution of vegetation cover on the landscapes. Further, the combination of orographic precipitation and spatially varied solar radiation created the highest divide migration due to the gentler windward side slopes than the leeward side of the domain. This suggests the erosive power of increasing runoff under orographic precipitation dominates the effect of vegetation protection on erosion on the windward side of the domain. The modelling outcomes from this study suggest that slope control radiation in combination with orographic precipitation plays a key role in the generation of topographic asymmetry in semi-arid ecosystems.

Keywords: Orographic precipitation, landscape evolution, topographic asymmetry, vegetation, semi-arid ecosystems

1. Introduction

Precipitation patterns in mountain ranges are strongly controlled by topography due to orographic lift mechanisms; and are also highly variable in space and persistent over long timescales (Anders et al., 2008; Houze et al., 2012). The phenomenon of orographic precipitation is usually more pronounced in mountain ranges at midlatitudes, where the prevailing winds are perpendicular to the mountains (Roe et al., 2002, 2003; Roe, 2005; Chaboureau et al., 2008; Kirshbaum and Smith, 2008; Minder, 2010; Colberg and Anders, 2014; Shi and Durran, 2015). Semi-arid regions are highly dependent on mountain water flow for their freshwater supply, as a large proportion of the available runoff is due to precipitation from high-elevation areas (Viviroli et al., 2007; Scaff et al., 2017). Henceforth, understanding the influence of precipitation-topography relationships in semi-arid ecosystems is critical towards quantifying the sensitivity of landscapes to changes in climate and vegetation cover.

Due to the effect of orographic precipitation, a wetter climate prevails on the windward side of a mountain flank compared to the leeward side of the mountain flank, as it receives less precipitation than the windward flank. Additionally, elevation also controls precipitation and enhances differences in microclimatic conditions, as the mean annual precipitation rate increases with elevation (Roe et al., 2002, 2003; Anders et al., 2006; Colberg and Anders, 2014; Garreaud et al., 2016) across a mountain range. Many researchers have studied the phenomenon of orographic precipitation across various study sites worldwide. For example, studies have been conducted on the Cherrapunji in the Khasi Hills, India's Himalayan range (Murata et al., 2007); the high central valley of Atacama Desert, Chile (Houston and Hartley, 2003); the Mauna Loa and Mauna Kea ranges over Hawaii (Carbone et al., 1998); in semi-arid northern New Mexico (Guan et al., 2005); the Southern Alps in New Zealand (Wratt et al., 1996); and across the Pacific Northwest in the United States (Luce et al., 2013).

The impacts of orographic precipitation on various earth surface processes and landscape evolution have been explored in previous studies using both observational data on natural landscapes (Ferrier et al., 2013; Goren et al., 2014; Han et al., 2014) and numerical experiments (Tucker and Slingerland, 1997; Whipple et al., 1999; Roe et al., 2002; Gasparini et al., 2008). Thiede et al. (2004) showed that orographic precipitation strongly influences erosion rates, affecting the long term evolution of topography in the Himalayas. Similar findings were reported by Clift et al. (2008), who found a clear correlation between Himalayan denudation rates and Asian monsoonal patterns. Anders et al. (2008) and Han et al. (2015) also reported that river network and elevation distribution are affected by the orographic influence of precipitation. Numerical simulations conducted by Goren et al. (2015) further showed orographic controls on landform evolution under the constant uplift and no vegetation component, revealing that windward slopes are longer and gentler than the leeward ones, due to the more runoff production which leads to enhanced erosion. A key aspect missing from these previous landscape evolution studies, however, is the effect of coevolving vegetation patterns under orographic precipitation conditions. It is essential to understand how vegetation-climate interactions can affect the landform asymmetry (Zavala et al., 2020; Smith and Bookhagen, 2021).

Vegetation plays a key role in landscape evolution, as it modulates geomorphic processes such as erosion and sediment transport (Langbein and Schumm, 1958; Wilson, 1973; Summerfield and Hulton, 1994; Moglen et al., 1998; Collins et al., 2004; Dietrich and Perron, 2006; Saco et al., 2007; Collins and Bras, 2008; Willgoose, 2018; Yetemen et al., 2015a, 2019). Early on, Langbein and Schumn (1958) quantified the non-linear relationship between precipitation and sediment yield using their landscape evolution model (LEM). They demonstrated that vegetation and precipitation exert competing effects, where precipitation increases erosion and

vegetation inhibits erosion. Moglen et al. (1998) extended this study by developing empirical relationships concerning erosion, vegetation, and climate to investigate the influence of climate change on drainage density. Using these empirical relationships they illustrated that, as the climate becomes wetter, vegetation becomes denser, offsetting the increase in erosion rates which could potentially result from increased runoff. Further work incorporating the effect of vegetation into LEMs has revealed an increase in dynamic equilibrium slopes with increased vegetation, which is due to an increase in resistance to sediment transport and erosion (Roering et al., 2003).

The effect of spatially heterogeneous vegetation patterns can be of particular importance when attempting to understand the effect of vegetation cover on erosion. An important example of heterogeneous patterns due to aspect-controlled vegetation differences are frequently observed on opposing hillslopes, and these can create variations in water-stress patterns across slopes, particularly in semi-arid regions (Gutiérrez-Jurado et al., 2013; Zhou et al., 2013; Yetemen et al., 2015a; Bass et al., 2017; Kumari et al., 2020). The dense vegetation cover on north-facing slopes (NFS) provides a more erosion-resistant surface, which minimises the effect of runoff. On the other hand, south-facing slopes (SFS) with sparser vegetation are prone to higher erosion (Istanbulluoglu et al., 2008). Such aspect-controlled vegetation differences have a pronounced influence on landscape morphology at the hillslope scale and can lead to differences in the way topography evolves over time (Carson and Kirkby, 1972; McMahon, 1998; Istanbulluoglu et al., 2008; Yetemen et al., 2015; Srivastava et al., 2021).

Several modelling studies (Collins et al., 2004; Istanbulluoglu and Bras, 2005; Collin and Bras, 2008; Collins and Bras, 2010; Yetemen et al., 2015a, b) have been conducted in which the vegetation-erosion coupling in LEMs was included. Collins et al. (2004) coupled the Channel-Hillslope Integrated Landscape Development (CHILD) LEM with vegetation-erosion

dynamics and found that incorporating the dynamic vegetation component improved the representation of the co-evolution of landforms. Istanbulluoglu and Bras (2005) used CHILD coupled with dynamic vegetation and found that a landscape simulated with dynamic vegetation closely resembles a natural landscape. Additional results from Collin and Bras (2008) using CHILD suggest an asymmetry in vegetation recovery. Vegetation growth rates for drier climates, were slower than for wetter climates, due to limited by water availability. Yetemen et al. (2015a, b) improved the LEM framework developed by Istanbulluoglu and Bras (2005) and Collins and Bras (2010), by incorporating the effect of spatial varied solar radiation, and showed that solar radiation is a major driver of topographic asymmetry in semi-arid landforms.

Despite the significant progress that has been made in relating earth surface processes and vegetation patterns to hillslope aspect and climate, the understanding of feedback mechanisms between vegetation and erosion in LEMs remain limited. For example, all of the studies modelling landform evolution under orographic precipitation were performed under the assumption of bare-soil conditions (e.g., Goren et al., 2014; Han et al., 2015; Zavala et al., 2020). As mentioned in previous paragraphs, topographic asymmetry in these studies was triggered by variations in precipitation between the windward and leeward sides of the mountain (i.e., in bare-soil conditions). However, predictions around topographic asymmetry can be complex and affected by the presence of vegetation cover. This is because there will be competition between shear stress due to increased runoff and vegetation protection on both the windward and leeward sides of the mountain that might affect topographic asymmetry (Willgoose, 2018). This type of effect can only be analysed in modelling studies by incorporating an aspect-controlled vegetation framework into LEMs and enabling the coevolution of landforms and vegetation under the effect of orographic precipitation.

This study constitutes the first attempt to better understand the role of orographic precipitation on the coevolution of landforms and aspect-controlled vegetation in semi-arid ecosystems. To achieve this goal, the modelling framework of the CHILD LEM (Tucker et al., 2001) coupled with the vegetation dynamics component was modified to incorporate modules for orographic and elevation control on precipitation patterns, as well as solar radiation patterns on vegetation and landscape evolution. To elucidate the role of solar radiation and different precipitation, several combinations of precipitation and solar radiation were used, which are discussed in the methodology section of this paper.

2. Detailed Model Structure

The CHILD LEM coupled with a vegetation dynamics component (i.e., the Bucket Grassland Model [BGM], which explicitly simulates above- and below-ground biomass) was used in this study. A detailed description of the geomorphic process, vegetation dynamics, and climate forcing are provided in the following sub-sections.

2.1 Geomorphic dynamics

Geomorphic processes are responsible for moving sediment across the basin. The continuity equation for sediment gives the rate of change in elevation after considering various geomorphic processes such as uplift, hillslope diffusion, and fluvial erosion (Tucker et al., 2001), as follows:

$$\frac{dz}{dt} = U - \nabla . q_d - F \qquad \text{(Eq. 1)}$$

where z [L] is elevation and t [T] is time. The first term on the right gives the uplift, U [LT^{-1}]; the second term states the divergence of volumetric sediment flux per unit width of hillslope

157 diffusion, q_d [LT^{-1}]; and the third term, F [LT^{-1}], provides the fluvial erosion function. The q_d

158 varies with slope (Roering et al., 1999), as follows:

159 $$q_d = \frac{K_d \nabla z}{1 - \left(\frac{|\nabla z|}{S_{cr}} \right)^2} \quad \text{(Eq. 2)}$$

160 where K_d is diffusivity [L^{2}T^{-1}] and S_{cr} is the critical hillslope gradient. The fluvial process, F,

161 is given as

162 $$F = \begin{cases} \nabla q_f, & \text{where } D_c > q_f \\ D_c & \text{elsewhere} \end{cases} \quad \text{(Eq. 3)}$$

163 where ∇q_f represents net divergence of sediment flux per unit width [LT^{-1}] and D_c is the

164 detachment capacity [LT^{-1}], which gives the maximum rate of local erosion. Both detachment

165 (D_c) and transport (q_f) capacity can be expressed as a power function of shear stress (Nearing

166 et al., 1999; Meyer-Peter and Müller, 1948). The D_c and q_f are given via equations 4 and 5,

167 respectively.

168 $$D_c = k_d \left(\tau_{eff} - \tau_{cr} \right)^{dc} \quad \text{(Eq. 4)}$$

169 $$q_f = k_f \left(\tau_{eff} - \tau_{cr} \right)^{fc} \quad \text{(Eq. 5)}$$

170 where k_d and dc are the detachment-limited erodibility coefficient and exponent, respectively

171 (Nearing et al., 1999); k_f and fc represent the transport-limited erodibility coefficient and

172 exponent, respectively (Meyer-Peter and Müller, 1948); τ_{eff} (Pa) represents the effective shear

stress; τ_{cr} is the critical shear stress for sediment transport; and, finally, τ_{eff} is represented by following Equation 6, which is provided by Istanbulluoglu et al. (2002):

$$\tau_{eff} = \rho_w \cdot g \cdot \frac{n_s^{\alpha}}{n^{\beta}} \cdot C^{\gamma} \cdot Q^{\delta} \cdot S^{\varepsilon} \quad \text{(Eq. 6)}$$

where ρ_w is the density of water; g is acceleration due to gravity; C is a shape constant and taken as 0.36 for parabolic cross-section; Q is runoff discharge; and S is local slope, where $\alpha = 1.5, \beta = 1.125, \gamma = 0.75, \delta = 0.375, \varepsilon = 0.8125$. τ_{eff} can also be approximated with the boundary shear stress (τ_{bs}) and scaled using the ratio of Manning's roughness coefficient of vegetation (n_v) and bare soil (n_s), as outlined by Laursen (1958) and Istanbulluoglu and Bras (2005) in Equation 7:

$$\tau_{eff} = \tau_{bs}\left(\frac{n_s}{n_s + n_v}\right)^{3/2} \quad \text{(Eq. 7)}$$

Roughness due to particular vegetation (n_v) is represented as a power function of its reference vegetation cover, V_R = 0.95, which has a roughness coefficient, n_{vR} = 0.5 (Istanbulluoglu and Bras, 2005), as follows:

$$n_v = n_{vR}\left(\frac{V}{V_R}\right)^{\omega} \quad \text{(Eq. 8)}$$

where ω is the parameter that quantifies the relation between vegetation roughness to surface vegetation cover.

189 *2.2 Vegetation dynamics*

190 Ecohydrologic vegetation dynamics in CHILD were simulated in this study for a single plant
191 functional type (i.e., grass) by using the single-layer BGM. The BGM represents uniform soil
192 moisture within the root zone and spatially distributes using laterally connected elements in the
193 direction of flow. Each model cell was covered by grass (live and dead) and bare soil fractions
194 and updated following every storm event. The net primary productivity (*NPP*) of grass biomass
195 (g/m^2) was calculated as a function of interstorm evapotranspiration (ET_a) and water use
196 efficiency (*WUE*) and then allocated to aboveground and belowground biomass compartments
197 (Swenson and Waring, 2006), as follows:

198 $$NPP = 0.75 \cdot (1-\mu) \cdot ET_a \cdot WUE \cdot \rho_w \cdot \omega \quad \text{(Eq. 9)}$$

199 where μ is the ratio of exchange of CO_2 from daytime to night time, ρ_w is density of water,
200 and ω is a conversion factor of CO_2 to dry biomass (kg DM/kg CO_2). The production of the
201 sum of above-ground and below-ground grass biomass at the ecosystem scale is related linearly
202 with ET_a through the use of *WUE* (the ratio of biomass produced by the plants to the amount
203 of water transpired by a plant). According to Fick's law, *WUE* (kg CO_2/kg H_2O) can be
204 represented consistent with Farquhar et al. (1989):

205 $$WUE = \frac{p_a\left(1-\frac{p_i}{p_a}\right)}{1.6\Delta e} \quad \text{(Eq. 10)}$$

206 where p_a and p_i are the ambient and intercellular partial pressures of CO_2, respectively; and
207 Δe is the change in the water vapour pressure inside the leaf and in the air, respectively.

208 Biomass (g DM m^{-2}) decays following first-order reaction kinetics, which is regulated by water
209 stress (Yetemen et al., 2015a). Two separate biomass states (compartments) were tracked:

green aboveground (B_g) and dead biomass (B_d). Based on ordinary differential equations, biomass components were modelled consistent with Montaldo et al. (2005), as follows:

$$\frac{dB_g}{dt} = NPP \cdot a_c - k_g B_g - k_i B_g \xi_s \quad \text{(Eq. 11)}$$

$$\frac{dB_d}{dt} = k_g B_d - k_h B_d \xi_d \quad \text{(Eq. 12)}$$

where a_c is the allocation coefficient; k_g and k_h represent decay coefficients for green and dead biomass, respectively; k_i is the coefficient for drought-induced foliage loss; ξ_d is a coefficient for climate influence on dead biomass; and ξ_s is a water stress function for green biomass. This was determined by following equation Laio et al. (2001).

$$\xi_s = \begin{cases} 0, & s^* \le s \\ \left(\frac{s^* - s}{s^* - s_w}\right)^4, & s_w \le s \le s^* \\ 1, & s \le s_w \end{cases} \quad \text{(Eq. 13)}$$

where, s [-] is degree of soil saturation, s_w and s^* are the soil moisture threshold levels for plant wilting point and reduced transpiration under plant water stress, respectively. The adjustment coefficient (ξ_d) for dead biomass and the allocation coefficient a_c were calculated, respectively, using the equations outlined by Istanbulluoglu et al. (2012):

$$\xi_d = \min\left(\frac{PET_i}{PET_{d\max}}, 1\right) \quad \text{(Eq. 14)}$$

$$a_c = \left(1 - \frac{LAI_g}{LAI_{\max} - LAI_d}, 1\right) \quad \text{(Eq. 15)}$$

225 PET_i is PET on the modelled day, and $PET_{d\max}$ is a constant for dead biomass loss adjustment.
226 The effect of temperature on the decomposition of dead biomass was incorporated via the ratio
227 of $\frac{PET_i}{PET_{d\max}}$ such that rate of decay is higher during warmer days.

228 In equations 16 and 17, LAI_g and LAI_d are green and dead LAI, respectively; and $LAI_{\max}$ is
229 the maximum LAI for a fully vegetated surface. The LAI values were estimated from the
230 biomass through the linear relationships, consistent with Arora, (2003):

231 $$LAI_g = B_g \cdot SLAI_g \quad \text{(Eq. 16)}$$

232 $$LAI_d = B_d \cdot SLAI_d \quad \text{(Eq. 17)}$$

233 where $SLAI_g$ and $SLAI_d$ are specific leaf area and the green and dead leaf area index,
234 respectively (Istanbulluoglu et al., 2012). The total leaf area index LAI_t was estimated by

235 $$LAI_t = SLAI_g + SLAI_d \quad \text{(Eq. 18)}$$

236 The vegetation cover fraction, V_t [-], for total biomass is represented by an exponential
237 function, as outlined by Lee (1992):

238 $$V_t = [1 - \exp(0.75 \cdot \mathrm{LAI}_t)] \quad \text{(Eq. 19)}$$

239

240 *2.3 Rainfall input*

241 The Poisson rectangular pulse (PRP) rainfall model was modified to incorporate into the
242 CHILD model to generate the stochastic rainfall forcing (Eagleson, 1978). Every storm event

is considered to have three essential characteristics: storm intensity (p) [LT^{-1}]; storm duration, T_r [T]; and interstorm period, T_b [T]. All three characteristics of the PRP model are best described by the exponential distribution given by Eagleson (1978):

$$f(p) = \frac{1}{\overline{p}} \exp\left(-\frac{p}{\overline{p}}\right) \quad \text{(Eq. 20)}$$

$$f(T_r) = \frac{1}{\overline{T_r}} \exp\left(-\frac{T_r}{\overline{T_r}}\right) \quad \text{(Eq. 21)}$$

$$f(T_b) = \frac{1}{\overline{T_b}} \exp\left(-\frac{T_b}{\overline{T_b}}\right) \quad \text{(Eq. 22)}$$

where $\overline{p}$, $\overline{T_b}$, and $\overline{T_r}$ represent the mean distribution of storm intensity (p), storm duration (T_r), and interstorm period T_b. The mean annual precipitation $(\overline{p})$ is expressed consistent with Collins and Bras (2010):

$$\overline{p} = p \cdot T_r \cdot N_s \quad \text{(Eq. 23)}$$

where N_s [-] is the number of storms in a year and is given by

$$N_s = \frac{1}{T_r + T_b} \quad \text{(Eq. 24)}$$

3. Methodology

The role of different precipitation settings on co-evolving landforms with vegetation cover is outlined in this study. To achieve this goal, the CHILD+BGM model was used, which was previously calibrated and validated using soil moisture, runoff, and satellite-based LAI data for the Sevilleta National Wildlife Refuge (SNWR) in central New Mexico (Yetemen et al., 2015a,

b). A brief overview of the synthetic domains and the design of the numerical experiments used in this study is presented below.

3.1 Synthetic domain

Figure 1 shows the two-dimensional (2D) synthetic domain used in the CHILD+BGM numerical LEM to explore the role of different rainfall settings on vegetation and landform co-evolution. This domain displays the main channels in the east-west direction in agreement with the general features of the SNWR (Gutiérrez-Jurado et al., 2007, 2013; Yetemen et al., 2015a; 2015b; Bass et al., 2017; Srivastava et al., 2021). The CHILD model was run on a 1000×4000 m triangulated irregular network domain constructed using 50 m regularly spaced nodes such that the fluxes of surface runoff and sediment were permitted through two open boundary downslope edges. As shown in Figure S1 of the supplementary material, the elevation was highest at 2000 m. All model simulations were run for 800,000 years so that the simulated landscapes attained dynamic equilibrium between erosion (E) and uplift ($E \cong U$), driven by U = 0.1 mm/year. The last 100-year period of elevation, erosion, and vegetation cover fraction (V_t) in each grid cell was used to examine differences in landform, erosion, and vegetation patterns resulting from the different precipitation and insolation settings.

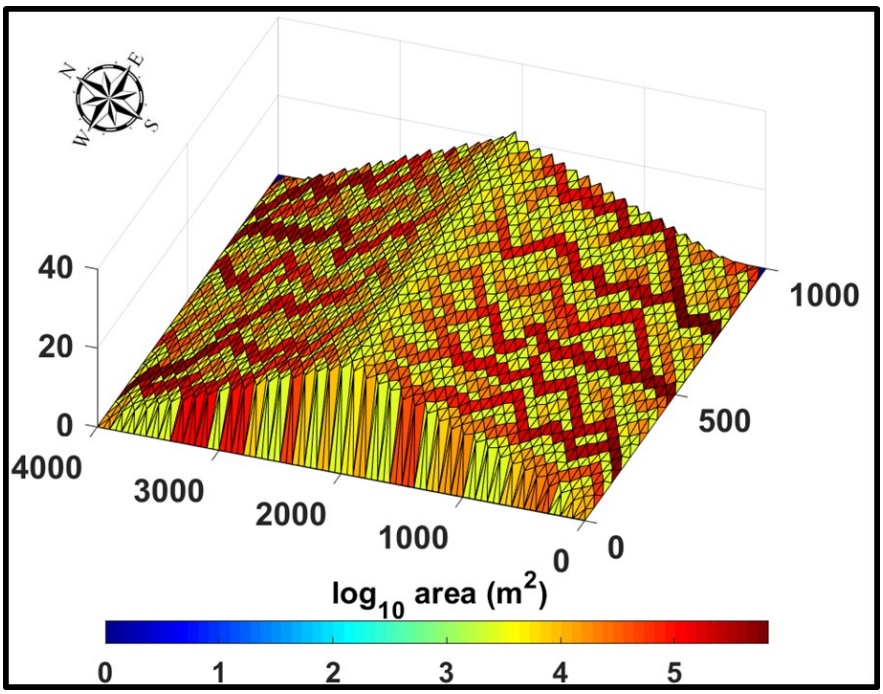

Figure 1: *Two-sided synthetic domain (showing contributing drainage area in m^2) used in the design of the numerical experiments in the current study.*

3.2 Numerical experimental settings

Several simulations were conducted using CHILD+BGM on the synthetic domain shown in Figure 1. Notably, in each simulation, soil and vegetation parameters were considered uniform over the entire domain. These simulations were conducted to understand the combined role of solar radiation and different precipitation settings on the co-evolution of vegetation patterns and semi-arid landforms. In total, six different scenarios were designed using a combination of two different solar radiation conditions and three different precipitation settings, as described below.

To elucidate the role of solar radiation on the spatial distribution of vegetation cover, two different scenarios were used: i) uniform radiation and ii) slope control on radiation. For uniform radiation, solar radiation was uniformly distributed as a function of day of the year

and latitude throughout the domain. In this scenario, every cell received the same amount of solar radiation corresponding to that of a flat surface on that day. In the spatial radiation case (slope control), solar radiation was spatially varied as a function of day of the year, latitude, aspect, and slope throughout the domain.

To investigate the role of different precipitation settings on the coevolution of vegetation and landform patterns, three different scenarios were designed: i) uniform precipitation, ii) elevation controlled precipitation, and iii) orographic precipitation. Figure 2 shows a schematic diagram for the spatial distribution of precipitation with distance across the synthetic domain for the three scenarios. In the uniform precipitation case, all grid cells recieved the same amount of precipitation, as shown in Figure 2a. In the elevation controlled precipitation case, precipitation was spatially varied as a function of elevation on both sides of the domain (Figure 2b). In the orographic precipitation scenario, the precipitation varied as a function of elevation differently on the windward and leeward sides of the domain. To distribute the precipitation over the landscape (Figure 2c), the precipitation was adjusted for the windward and leeward sides using a linear relation. Linear models for orographic control on precipitation are simple and have previously been used in the literature (Osborn, 1984; Wainwright, 2005; Nearing et al., 2015). The modelled precipitation P_z at a cell with elevation (Z_i) was obtained using the following equation:

$$P_z = P\left[\left(1+\frac{Z_i - Z_o}{Z_{\max} - Z_o}\right)P_{wind} + AspF\left(\frac{Z_{\max} - Z_i}{Z_{\max} - Z_o}\right)P_{lee}\right] \quad \text{(Eq. 25)}$$

where P is the precipitation at Z_o, P_{wind} [m^{-1}] is the windward orographic precipitation fraction, and P_{lee} [m^{-1}] is the leeward orographic precipitation fraction. The precipitation was scaled linearly as a function of the elevation and windward and leeward fractions (P_{wind} = 1 and P_{lee} =

312 0.5), as shown in Figure 2c. Z_i represents the cell elevation [m], Z_o is the initial elevation [m],
313 and $Z_{\max}$ is the maximum elevation [m]. $AspF$ is a factor [-], which defines on which side of
314 the mountain range the cell is (i.e., windward or leeward), where *AspF* is

315 $$AspF = \begin{cases} 0, \text{windward} \\ -1, \text{leeward} \end{cases}$$

316 Based on the Equation 25, the distributions of the modelled precipitation cases which were
317 considered in the simulations are shown on the landscapes in Figure 2 and Figure S1 (in the
318 Supplementary material). In this case, where precipitation at the initial elevation was 400 mm,
319 it increased as a function of elevation, leading to a maximum precipitation of 800 mm at the
320 highest elevation. P_{lee} was found to be lower than the P_{wind}, which indicates that the low
321 elevations on the leeward side received less precipitation (200 mm) compared with those on
322 the windward side. The linear orographic precipitation model provides an idealised
323 representation of the relationship between precipitation and topography and has successfully
324 been used in many climatological studies (Smith et al., 2003; Smith and Barstad, 2004; Anders
325 et al., 2006; Minder, 2010; Lundquist et al., 2010).

326 The experiments were carried out by combining the three precipitation settings and two solar
327 radiation conditions. To quantify how the landscape would evolve in response to different
328 precipitation patterns only, a set of experiments with uniform solar radiation were run using a)
329 uniform, b) elevation control, and c) orographic precipitation. A set of three experiments were
330 also conducted with slope control on radiation driven by d) uniform, e) elevation control, and
331 f) orographic precipitation. The experiment with slope control on radiation and uniform
332 precipitation was pursued to single out the role of aspect on the coevolving landscape. The
333 results for the six scenarios are outlined in the following section.

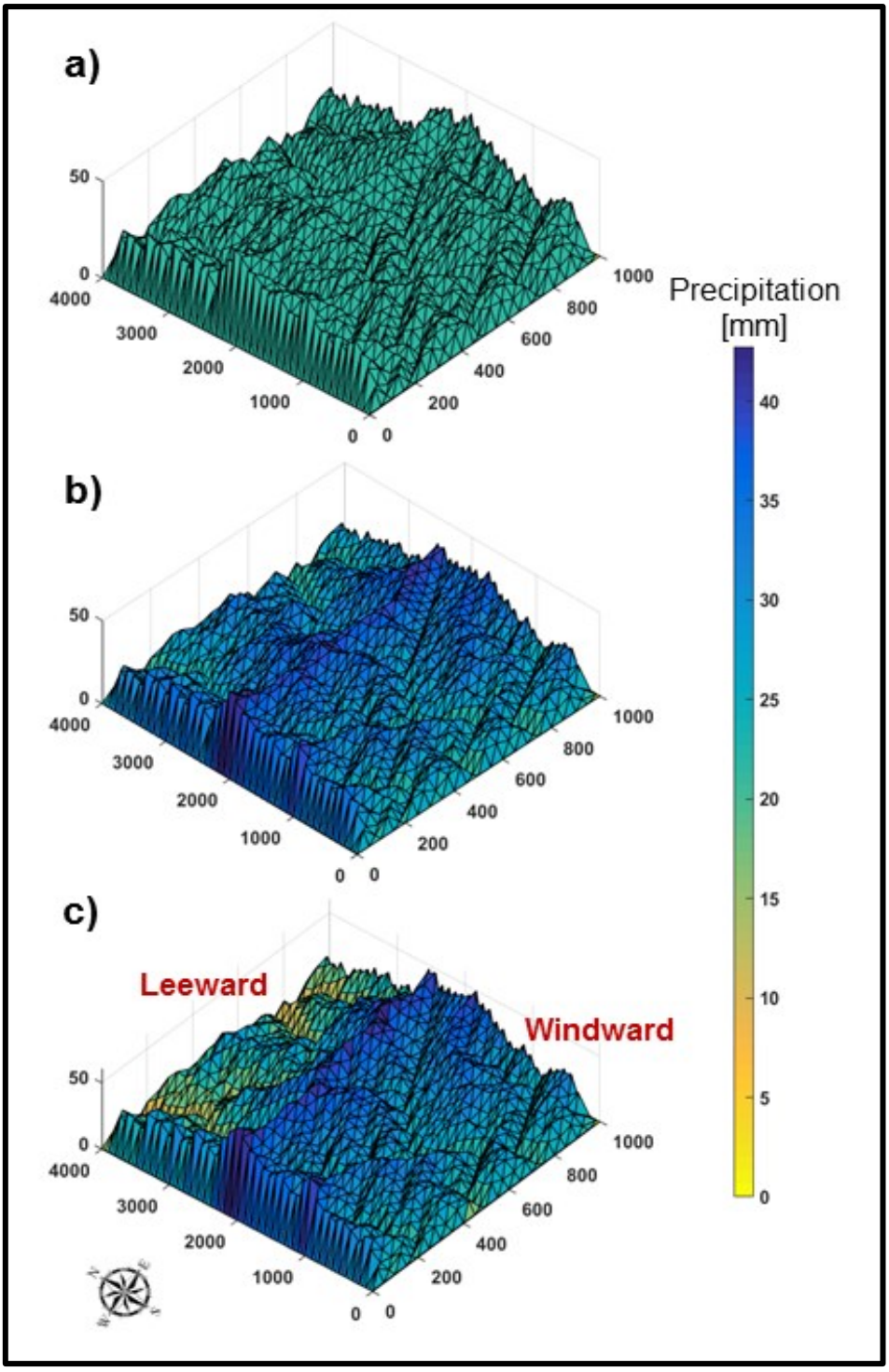

334

335 ***Figure 2:*** *Spatial distribution of three different precipitation settings: a) uniform precipitation,*

336 *b) elevation controlled precipitation, and c) orographic precipitation at a particular time step*

337 *of the year.*

338

4. Results

4.1 Influence of different precipitation and radiation patterns on the spatial distribution of vegetation cover

The spatial patterns of simulated vegetation cover for the six combinations of precipitation and radiation scenarios are provided in Figure 3 (3-dimensional plots of spatial vegetation cover for these settings are provided in Figure S2, in the Supplementary material). The spatial pattern of simulated vegetation cover for the uniform solar radiation and uniform precipitation scenario is shown in Figure 3a. The vegetation cover fraction was found to reach a value of 0.45 in this scenario. The higher values of the vegetation cover fraction occurred in the channels (higher contributing areas). This highlights a dominant network control on vegetation patterns for this scenario, since the incoming solar radiation and precipitation were uniform. Therefore, the only observed spatial variability in vegetation distribution in this case was due to the effect of enhanced soil moisture in areas of flow concentration.

The spatial pattern of the mean simulated vegetation cover fraction for the uniform solar radiation setting in combination with elevation control precipitation is shown in Figure 3b. Higher vegetation cover (darker green pixels) can be seen in the middle of the domain (~1500–2500 m) where elevation is high. This shows the elevation control on the vegetation cover pattern, as vegetation cover increased in areas of high precipitation. This is also reflected in the higher amount of vegetation cover fraction which, for this scenario, reached ~0.65 at high elevations. Areas with lower elevations on both sides of the domain, which received comparatively less precipitation, were found to have a lower vegetation cover (i.e., ~0.45). Notably, this pattern of elevation control was found to be so strong that it completely counteracted the effect of the network.

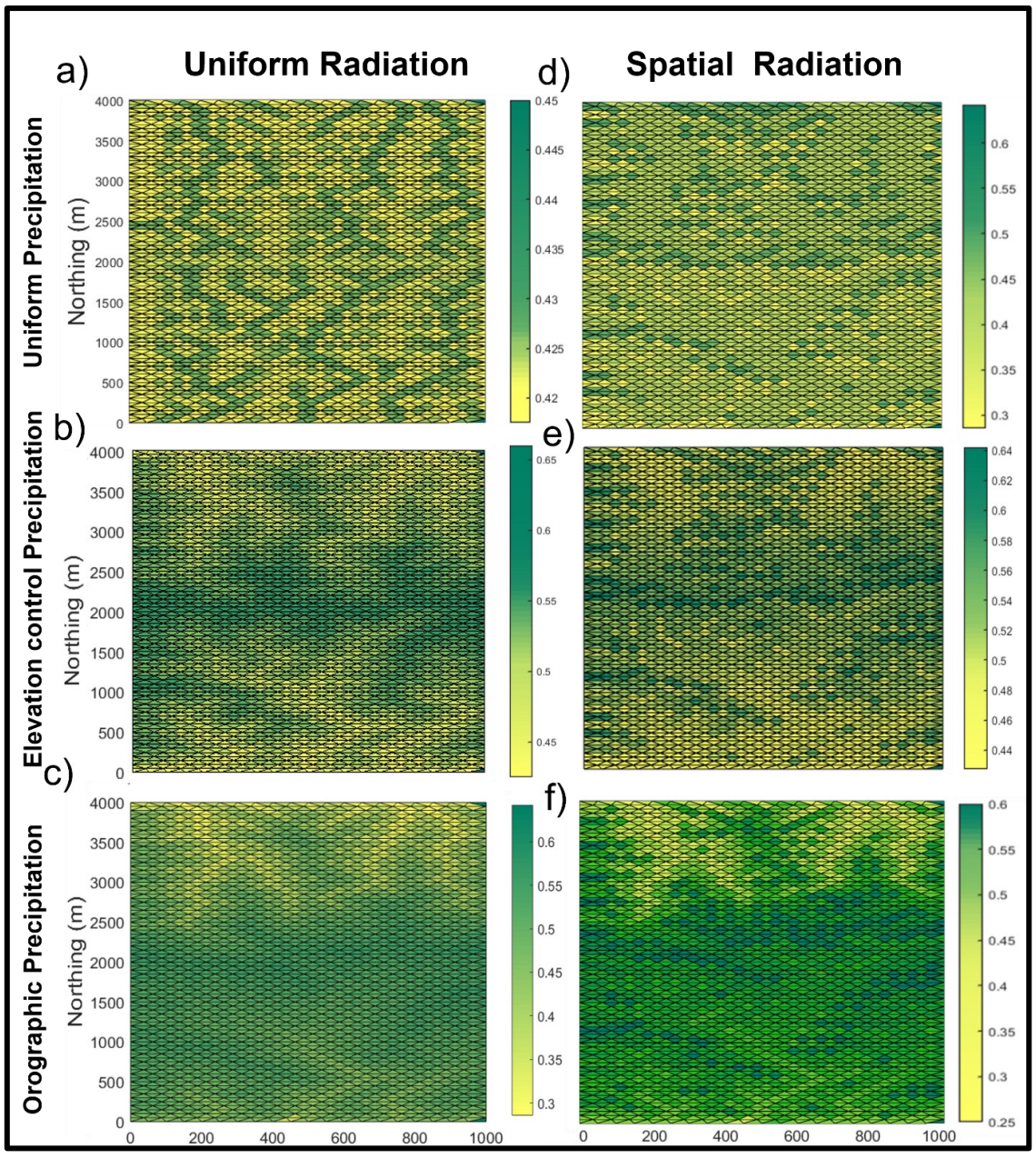

362

363 ***Figure 3:*** *Spatial patterns of the simulated vegetation cover fraction (mean values over the*
364 *last 100-year period) for the different precipitation and solar radiation scenarios. The left*
365 *panel (first column) shows the results for the uniform solar radiation scenario for a) uniform*
366 *precipitation, b) elevation control precipitation, and c) orographic precipitation. The right*
367 *panel (second column) shows the spatially varied solar radiation scenario for the three*
368 *precipitation patterns. Note that the range of values (colour bands) varies for different*
369 *scenarios, which was necessary for pattern visualisation.*

Figure 3c shows the spatial pattern of the mean vegetation cover fraction for simulations with orographic precipitation and uniform solar radiation inputs. Unlike the previous two settings, the amount of vegetation cover was found to be higher on the windward side of the domain (0–2000 m) than in the leeward side (2000–4000 m) due to the orography effect, as there was higher rainfall on the windward side (this is also visible in the 3-dimensional plots, as shown in Figure S1c in the Supplementary material). As in the previous case, the effect of increased vegetation in higher elevation (with higher precipitation) also characterises this pattern.

The spatial pattern of mean simulated vegetation cover for spatially varied solar radiation in combination with uniform precipitation is presented in Figure 3d. A higher range of vegetation cover fraction values (~0.3–0.6) was obtained in this case when compared with those from the uniform solar radiation scenario. The distinct differences between the patterns shown in Figures 3a and 3d suggest that the spatial variability of solar radiation and its associated aspect-driven effects dominated the vegetation response (the aspect distribution is shown in Figure S3 in the Supplementary material). A similar spatial pattern of vegetation was observed in the case of spatially varied solar radiation combined with elevation controlled precipitation, as shown in Figure 3e. However, in this case, the pattern was found to clearly reflect not only the radiation control but also the elevation control on precipitation. The aspect control is reflected by the presence of a higher vegetation cover fraction on the NFS; in this case, however, a higher vegetation cover fraction can be observed at higher elevations. This last observation becomes evident when Figures 3e to 3d are compared.

Lastly, Figure 3f shows the spatial pattern of simulated vegetation cover fraction for the spatially varied solar radiation under orographic precipitation input. In this case, the pattern can be seen to resemble the same features in the two previous cases (Figures 3e and 3d) but with the effect induced by the existence of higher precipitation on the windward side. First, the

windward side was found to have higher vegetation cover fraction compared with the leeward side of the domain. Second, the aspect control of solar radiation was also evident in this pattern. Moreover, it can also be observed that the NFS on the windward side has a higher vegetation cover fraction compared with the NFS on the leeward side due to the effect of orographic precipitation. The role of aspect and elevation on the simulated vegetation cover fraction on different precipitation settings is described in more detail in the next sub-section.

4.2 Vegetation cover fraction as a function of elevation and aspect

To explore the effect of aspect, the pixels were classified as North = 315°–360° and 0°–45°, East = 45°–135°, South = 135°–225°, and West = 225°–315°. Figure 4 shows scatter plots of the mean total vegetation cover fraction as a function of elevation for the three different precipitation distributions (i.e., uniform, elevation control, and orographic) considering spatial variability in solar radiation.

The mean total vegetation cover as a function of elevation for the NFS and SFS for the scenario with uniform precipitation is presented in Figure 4a. Vegetation cover in this case did not change significantly with elevation as precipitation was uniformly distributed. These trends are produced by the effect of slope angle. As a result of differences in insolation, NFS (which have lower evapotranspiration) were found to have a denser canopy compared with SFS. Upper hillslope areas are usually steeper (as will be discussed in more detail in later sections), which affects insolation. Steep NFS have lower insolation than gentle slopes, while steep SFS have higher insolation than gentle ones which explains the trends observed for higher elevations, as areas with higher insolation have higher evaporation and lower soil moisture, which therefore sustains reduced vegetation cover. Figure 4b shows the mean vegetation cover as a function of elevation under the combined effect of spatially varied radiation and elevation control on

417 precipitation. Similar to the previous scenario, NFS had higher vegetation cover than the SFS,
418 but in this case, vegetation cover increased as a function of elevation. Mean vegetation cover
419 ranged from 0.32 to 0.5 for the NFS, while it ranged from 0.32 to 0.41 for the SFS.

420 The mean vegetation cover fraction as a function of elevation for the case of orographic
421 precipitation and spatially varied radiation is shown in Figure 4c, which displays differences
422 for the NFS and SFS on the windward and leeward sides of the domain. The highest values for
423 the vegetation cover fraction were found for cells with a north windward (~0.5) position. These
424 values were always above those for cells with the same elevation but located in the north
425 leeward, south windward, and south leeward positions. Unlike the previous two precipitation
426 settings, the relationship between the vegetation cover and elevation was more complex for
427 this scenario due to competition between solar radiation and precipitation on the windward and
428 leeward sides of the domain. The lowest vegetation cover fraction was observed on the SFS at
429 the leeward side of the domain due to soil moisture stress induced by solar radiation and the
430 orographic shade effect. It was also found that the lower elevation of the NFS on the leeward
431 side had a lower vegetation cover fraction, while the SFS on the windward side had a higher
432 vegetation cover fraction. This is due to the effect of orographic precipitation in the case
433 analysed (due to the assumed wind direction). However, at higher elevations (> 30 m), the NFS
434 on the leeward side had a higher vegetation cover fraction than the SFS on the windward side
435 of the domain. This occurred because, at higher elevations, the precipitation was similar on
436 both sides, and the role of solar radiation intensified. Overall, vegetation patterns are strongly
437 affected by rainfall patterns and variability in solar radiation.

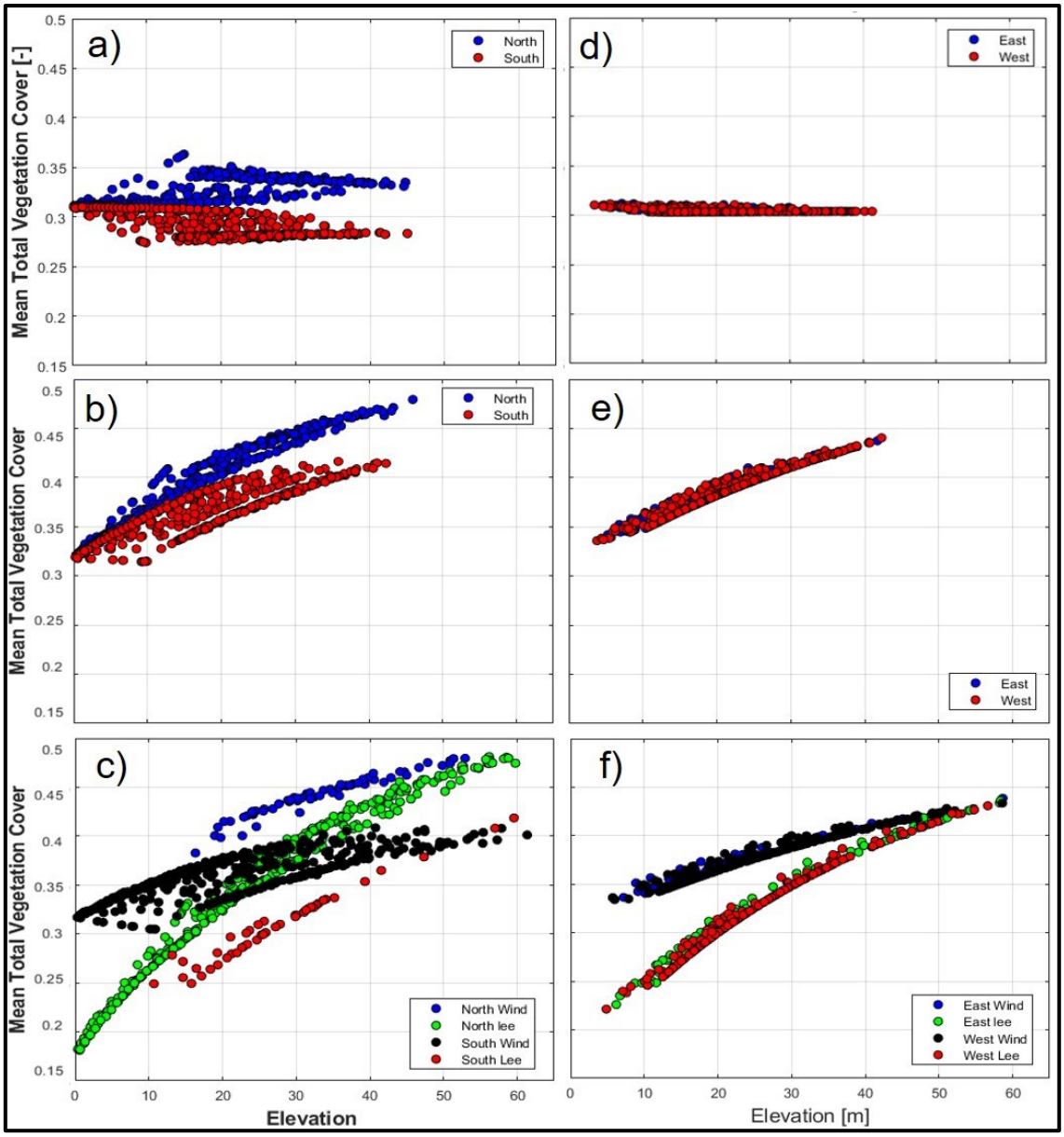

438

439 ***Figure 4:*** *Simulated mean total vegetation cover as a function of elevation on NFS and SFS*
440 *(first panel) and EFS and WFS (second panel) for different precipitation settings: a) uniform*
441 *precipitation, b) elevation control precipitation, c) orographic precipitation. The NFS and SFS*
442 *on the windward side are represented by 'North Wind' and 'South Wind', respectively. While*
443 *the NFS and SFS on the leeward side of the synthetic domain are illustrated by 'North Lee'*
444 *and 'South Lee', respectively. The EFS and WFS on the windward side are represented by*
445 *'East Wind' and 'West Wind', respectively, and the EFS and WFS on the leeward side of the*
446 *synthetic domain are illustrated by 'East Lee' and 'West Lee', respectively.*

Figure 4d shows the mean vegetation cover as a function of elevation for east-facing slopes (EFS) and west-facing slopes (WFS) for the uniform precipitation and spatially varied solar radiation setting. EFS and WFS had a similar amount of the vegetation cover fraction (~0.31) across the whole elevation range. The role of aspect was not significant on the EFS and WFS and was similar to that for a flat surface. Figure 4e shows the mean vegetation cover fraction plotted as a function of elevation for the elevation control precipitation and spatial varied solar radiation setting, which reflects the increase in rainfall with elevation, but, again, shows no differences in vegetation cover between EFS and WFS at the same elevation. Figure 4f shows that when considering the effect of orographic precipitation, it can be observed that although there was no difference in the vegetation cover at the EFS and WFS within the windward and leeward sides of the domain, vegetation cover increased with elevation. Additionally, EFS and WFS on the windward side were found to support higher vegetation cover than the EFS and WFS on the leeward side of the domain due to the influence of orographic precipitation.

4.3 Influence of different precipitation and solar radiation settings on divide migration

Figure 5 displays the development of topographic asymmetry over the geologic time scales for all of the study cases. Figure 5a shows the case with uniform precipitation and uniform radiation, where no divide migration is visible, as an almost negligible number of pixels shifted. On the other hand, when precipitation is uniform but solar radiation varies spatially due to the effect of aspect (Figure 5d), it can be seen that a few pixels tend to migrate. This is likely due to the role of differences in radiation which creates differences in vegetation distribution on hillslopes with different aspects. Figures 5b and 5e show a similar pattern for elevation controlled precipitation but with a larger number of pixels shifting. In this case, the role of spatially varied solar radiation intensified (Figure 5e), inducing higher divide migration than in the case of the elevation controlled precipitation with uniform solar radiation (Figure

5b). Figures 5c and 5f show that the divide migration is more pronounced for the orographic precipitation case with both spatial and uniform solar radiation. However, among these last two cases, the divide migration phenomenon was again enhanced when the effect of aspect-controlled solar radiation was considered (Figure 5f). This is due to the combined effect of aspect driven vegetation differences and rain shadow effects. This shows that the aspect influence on topographic asymmetry is more pronounced in combination with the influence of orographic precipitation. The effect of topographic asymmetry presented in Figure 5 is further explored by examining the elevation maps (Figure 6) and slope-area diagrams (Figure 7), as discussed below.

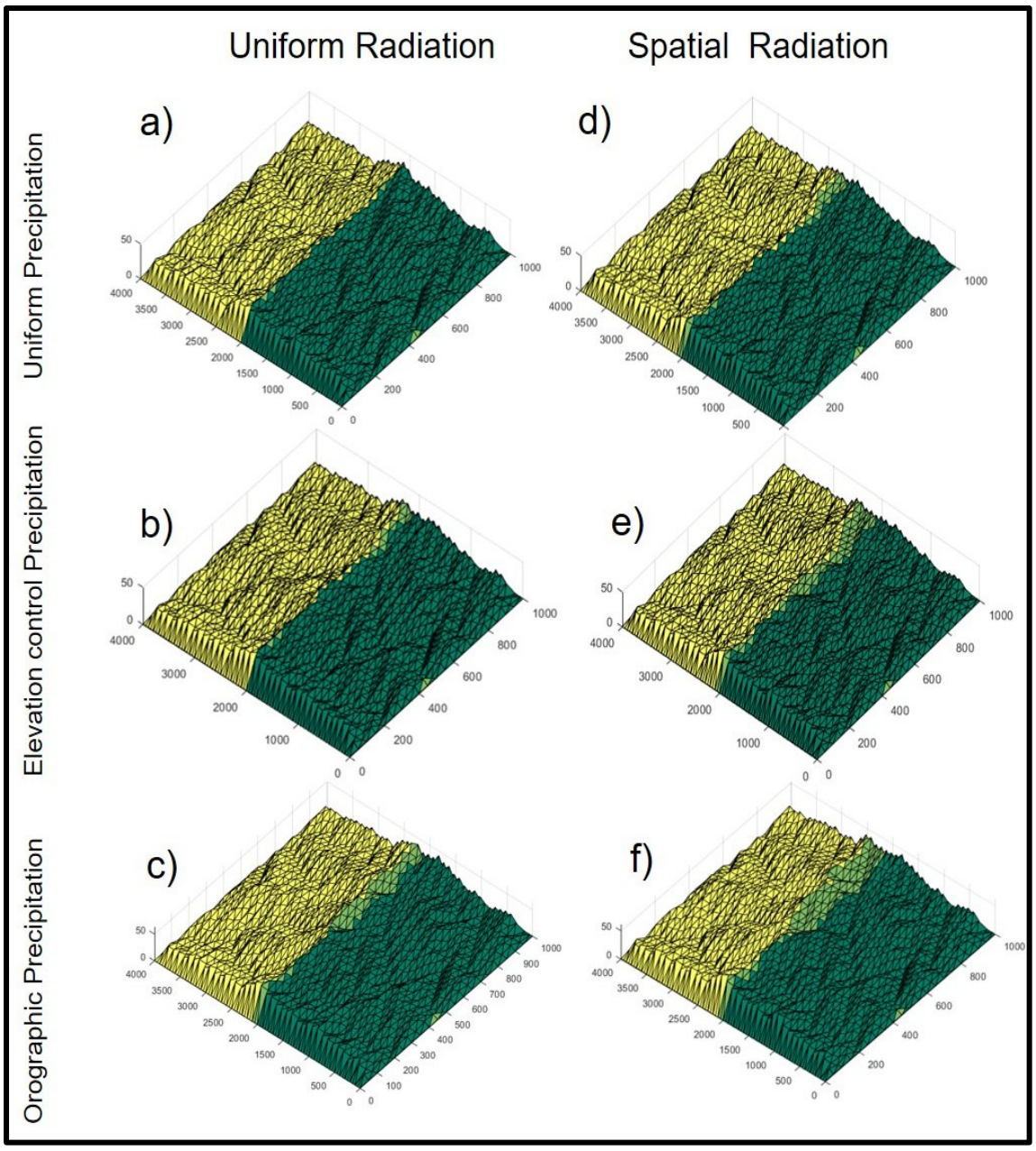

Figure 5: *Modelled divide migration map from CHILD for different precipitation and solar radiation cases. The left column of the diagram shows the uniform solar radiation cases for a) uniform precipitation, b) elevation control precipitation, and c) orographic precipitation. The right column of the diagram shows the spatial radiation cases for d) uniform precipitation, e) elevation control precipitation, and f) orographic precipitation. Green represents the windward side of the domain and yellow represents the leeward side with respect to orographic precipitation. Finally, the light green indicates the migration of the pixels.*

Elevation was found to increase to ~45 m for the cases of uniform and elevation control precipitation with uniform radiation, which were found to have almost no divide migration (Figures 6a and 6b). It can also be observed that there were negligible differences in the mean slopes at both sides of the domain (Figures 7a and 7b) in both of these cases. Though there was minimal difference in the elevation for uniform precipitation and elevation control precipitation for the spatially varied radiation case (Figure 6d–e), Figures 7d and 7e show some subtle differences, with the slopes on the leeward side being slightly steeper than those on the windward side of the domain, particularly for the case that accounts for aspect driven radiation effects (displaying a higher number of migrating pixels in Figure 5). When orographic precipitation was considered (Figures 6c and 6f), the simulated elevations at the divide tended to be higher than those from the other precipitation scenarios, increasing to ~60 m for both simulations with uniform and spatially varied solar radiation. Figures 7c and 7f show that the slopes of the leeward face were steeper than the windward slopes of the domain. Among the two cases of orographic precipitation, the differences on the windward and leeward slopes were found to be more pronounced in the spatially varied solar radiation case.

To capture and compare the trends in divide migration simulated and discussed in previous studies (Goren et al., 2014; Han et al., 2015) with the results obtained in the current study (which accounted for vegetated landscapes), simulations for bare soil conditions were also run. Importantly, the simulations with bare soil, using spatially varied radiation and orographic precipitation settings, displayed less divide migration than the simulations using the same scenario but including dynamic vegetation cover (Figure S4 in the Supplementary material).

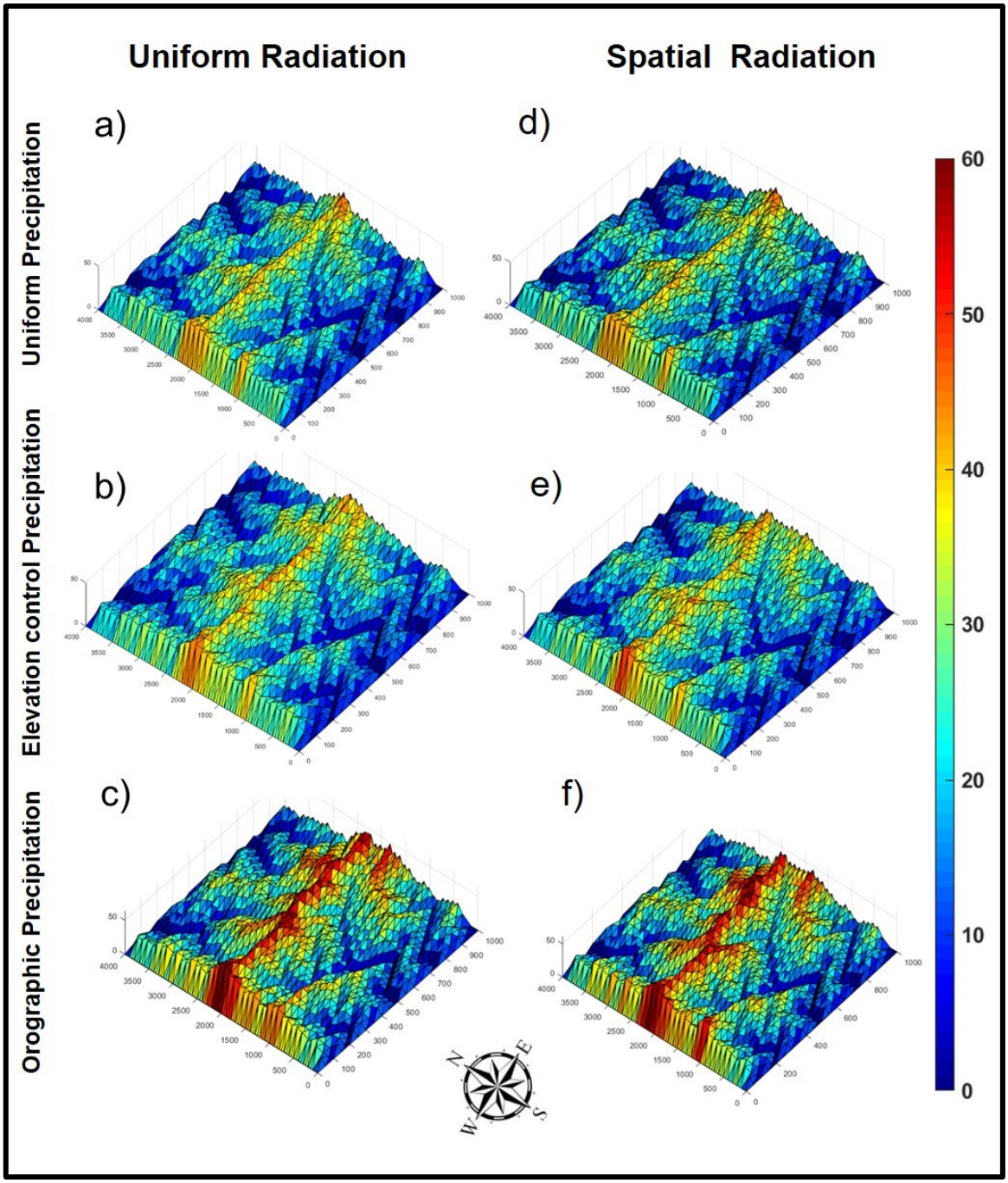

509

510 ***Figure 6:*** *Three-dimensional views of modelled elevation map from the CHILD model for*
511 *different precipitation and solar radiation cases. The modelled elevation map is plotted on*
512 *evolved topography, where the left column of the diagram shows the uniform solar radiation*
513 *cases for a) uniform precipitation, b) elevation control precipitation, and c) orographic*
514 *precipitation. The right column of the diagram shows the spatially varied solar radiation cases*
515 *for d) uniform precipitation, e) elevation control precipitation, and f) orographic precipitation.*

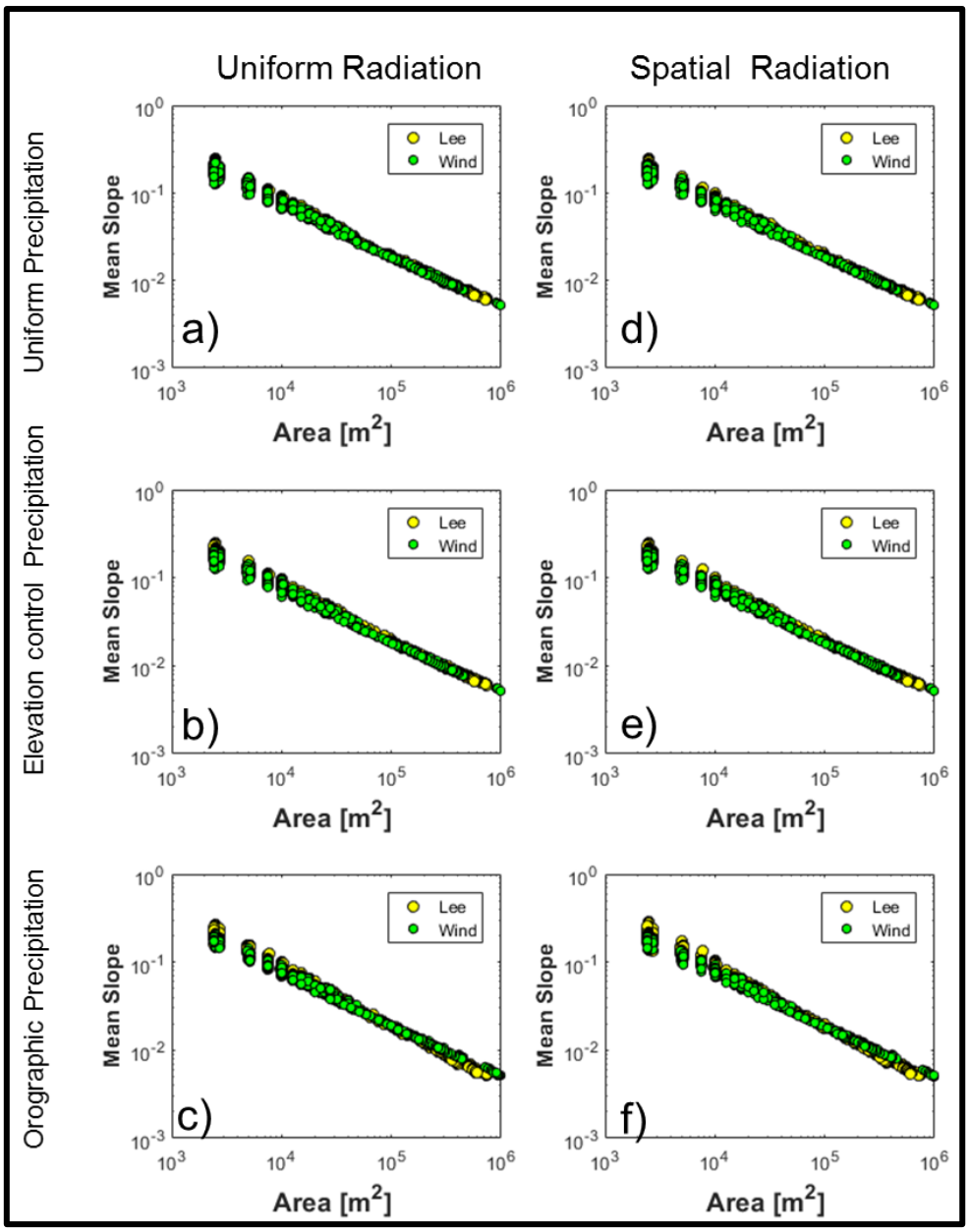

516
517

518 ***Figure 7:*** *Slope-area relationship of the modelled landscapes for different precipitation and*
519 *solar radiation cases. The left column of the diagram shows the uniform solar radiation cases*
520 *for a) uniform precipitation, b) elevation control precipitation, and c) orographic*
521 *precipitation. The right column of the diagram shows the spatially varied solar radiation cases*
522 *for d) uniform precipitation, e) elevation control precipitation, and f) orographic precipitation.*

523
524

Figure 8 displays the results for the slope-area diagram for the orographic precipitation and spatially varied solar radiation scenario for both vegetated and bare soil conditions. It was found that the slopes on the windward and leeward sides of the domain with vegetation cover were always higher than the windward and leeward slopes of the bare soil domain. As discussed in previous sections, the leeward slopes for the vegetated domain were steeper than the windward slopes. In a similar fashion, the leeward slopes of the bare soil domain were found to be steeper than those at the windward flank throughout the domain.

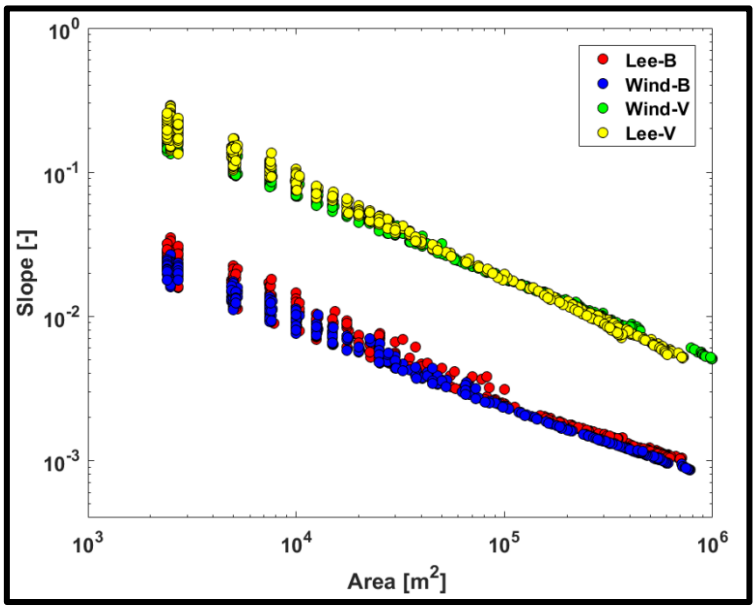

Figure 8: *Slope-area plot for orographic precipitation with bare soil and vegetated domains for the windward and leeward slopes. 'Lee B' and 'Wind B' represent the mean slopes of the bare soil on the leeward and windward sides of the domain, respectively, and 'Wind V' and 'Lee V' represent the mean slopes of the windward and leeward sides of the domain, respectively.*

Figure 9 shows the discharge for the windward and leeward sides using the orographic precipitation with the spatially varied solar radiation setting for both the vegetated and bare soil domains. The discharge for the windward side of the bare soil domain was found to be

541 higher than the windward side of the vegetated soil domain. Discharge for the leeward side of
542 the bare soil case was higher than the discharge of the leeward side for the vegetated soil case.
543 The discharge was also higher on the windward side for both the bare soil domain and vegetated
544 domain in comparison to their respective leeward sides. From Figure S5 (in the Supplementary
545 material), it can be seen that the windward side of the vegetated domain had a higher
546 contributing area than leeward side, implying that the windward is gentler than leeward for the
547 case of orographic precipitation.

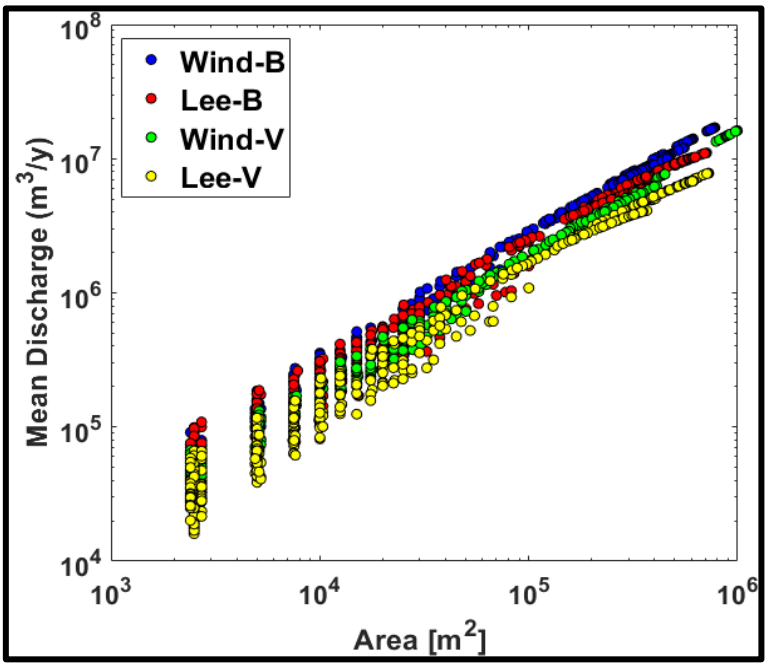

548

549 ***Figure 9:*** *Mean discharge-area plot for orographic precipitation with bare soil and vegetated*
550 *domain. 'Lee B' and 'Wind B' represent the mean discharge on the leeward and windward*
551 *sides of the bare soil domain, respectively, and 'Wind V' and 'Lee V' represent the mean*
552 *discharge of the windward and leeward sides of the vegetated domain, respectively.*

553 **5. Discussion**

554 Based on the simulations presented in previous sections, drainage network, aspect, and
555 elevation controls were identified as the three main drivers of vegetation patterns on the

landscape following the use of six different scenarios corresponding to the combination of uniform and spatially varied solar radiation with uniform, elevation control, and orographic precipitation. A higher simulated vegetation cover fraction was obtained for the channels (higher drainage areas) than the hillslopes for the case of uniform solar radiation and uniform precipitation settings. This highlights the strong control of network patterns on vegetation cover due to the flow concentration for this case. Since the incoming solar radiation and precipitation were uniform in this scenario (except for the channels that have higher contributing areas, there was little variation in vegetation cover across the rest of the domain, which is consistent with findings of previous studies (Istanbulluoglu et al., 2008; Yetemen et al., 2010 Yetemen et al., 2015a).

The control of aspect and slope on solar radiation was found to have a significant impact on vegetation cover for all of the precipitation settings (i.e., uniform, elevation control, and orographic precipitation) analysed. Differences in incoming solar radiation on the NFS and SFS led to differences in vegetation cover on these slopes. The strong role of aspect on vegetation pattern differences is consistent with that reported in previous studies showing that incoming solar radiation leads to sparser vegetation cover on the SFS than in the NFS (Broza et al., 2004; Caylor et al., 2004; Zou et al., 2007; Gutiérrez-Jurado et al., 2013; Hinckley et al., 2014; Flores-Cervantes et al., 2014; Yetemen et al., 2015a; Bass et al., 2017; Kumari et al., 2019; Srivastava et al., 2019).

The elevation and orographic precipitation controls led to higher vegetation cover at higher elevations due to an increase in precipitation with elevation. This is based on the observation that orographic effects on clouds and precipitating often results in greater precipitation at higher elevations, where temperatures are cooler and more precipitable water can accumulate (Roe, 2003; Giambelluca et al., 2011; Houze, 2012). Field and modelling studies have shown this

580 strong orographic effect on precipitation as a function of elevation at various locations (Hay
581 and McCabe, 1998; Hanson, 2001; Dettinger et al., 2004; Girotto et al., 2014; Kirchner et al.,
582 2014; Knowles et al., 2015). For instance, Dettinger et al. (2004) showed that precipitation at
583 higher elevation can be as much as 30 times more than at the base of the range. In this study,
584 the effect of orographic precipitation led to significant differences in vegetation cover,
585 particularly for the case in which slope controlled radiation area was considered. For this case,
586 the NFS and SFS on the windward and leeward slopes displayed highly distinct vegetation
587 cover values as a function of variations in both elevation and aspect, which is consistent with
588 results reported in previous studies (Elder et al., 1991; Winstral et al., 2013; Yetemen et al.,
589 2015a). Our results accounting for orographic rainfall effects that led to higher vegetation cover
590 on the windward side are also consistent with observations in field-based studies (Chen et al.,
591 1997; Giambelluca et al., 2011).

592 Indeed, the asymmetry caused by insolation was also found to be an effective variable driving
593 the vegetation pattern on the windward and leeward sides (Rozas et al., 2011). The results from
594 this study also highlight that it is very important to understand and recognise the combined
595 effects of slope aspect and predominant wind direction. This study demonstrated that the NFS
596 on the leeward side of the mountain flank hold a lower vegetation cover fraction than the NFS
597 on the windward side. However, denser vegetation cover existed on the SFS of the windward
598 side of the mountain flank—this is due to the direction of wind, which is assumed to come
599 from South direction. The effect of the windward versus leeward location can sometimes be
600 more important than location in terms of aspect, as shown in the studies by Dettinger et al.
601 (2004) and Lundquist et al. (2010) at Sierra Nevada of California.

602 The results from the bare-soil simulation show that the windward side of the domain was
603 gentler compared with the leeward side, which is consistent with the previous modelling studies

604 in which the influence of orographic precipitation was simulated for bare landscapes (Goren et
605 al., 2014; Han et al., 2015; Zavala et al., 2020; Paik and Kim, 2020). The study conducted by
606 Goren et al. (2014) showed that the windward side was longer than the leeward side of the
607 mountain due to higher rainfall leading to higher erosion rates. Therefore, it was found that
608 windward side of the mountain becomes gentler, whereas the other side (leeward) receives less
609 rainfall, in turn leading to steeper slopes under landform evolution equilibrium conditions (i.e.,
610 when erosion equals tectonic uplift).

611 Further, the current study also compared and contrasted the differences in divide migration for
612 a vegetated domain. Notably, the pattern found from the modelling results for the vegetated
613 domain remained consistent with that for the bare-soil domain, such that the windward side of
614 the domain was found to be gentler. One potential explanation for this pattern is that, though
615 the windward side had denser vegetation cover, the runoff discharge was higher on that side as
616 compared to the leeward side (Figure 9). This can lead to higher shear stress due to increased
617 runoff, with the results suggesting that the effect of higher shear stress dominates those of
618 vegetation protection on the windward side and leads to a decrease in topographic slope, as
619 shown in Figure 8 (Istanbulluoglu and Bras, 2005; Istanbulluoglu et al., 2008; Yetemen et al.,
620 2015a). Higher slopes were observed for the leeward side of the vegetated landscape, whereas
621 lower slopes were observed for the windward side. This topographic asymmetry between the
622 leeward and windward sides was found to be more pronounced for aspect-controlled and
623 orographic-precipitation conditions. This is because the effect of increased runoff dominates
624 that of vegetation protection on erosion on the windward side of the domain.

625

6. Conclusions

In this study, the CHILD LEM coupled with the vegetation dynamic component BGM was used to better understand the role of elevation controlled and orographic precipitation on the coevolution of landforms and aspect-controlled vegetation in semi-arid ecosystems. The results from the simulations showed that for uniform precipitation and uniform solar radiation, the vegetation pattern was controlled by the effect of the drainage network, as higher vegetation was observed in the channels. However, when the effect of aspect on radiation was considered, this effect became dominant. When elevation control on precipitation was considered under the assumption of uniform solar radiation, higher vegetation cover was observed at a higher elevation. However, when elevation control precipitation was combined with the effect of spatially varied solar radiation, the role of aspect was seen in addition to the elevation control phenomenon.

Unlike previous simulations, the results accounting for the orographic effect on precipitation and assuming uniform solar radiation showed denser vegetation cover on the windward than in the leeward side of the domain. On the other hand, when considering the effects of both orographic precipitation and spatially varied solar radiation, a more complex relationship was observed between vegetation and elevation, as there was competition between the effects of slope-controlled solar radiation and orographic precipitation on both sides of the domain. However, at higher elevations, where precipitation was similar on both sides, the slope control solar radiation effect dominated, leading to denser vegetation cover on the NFS on the leeward side compared with the SFS on the windward side of domain.

Differences in the coevolution of landforms under different precipitation and solar radiation settings were also significant and led to various degrees of topographic asymmetry. There was

649 negligible divide migration for the case of uniform precipitation and uniform solar radiation;
650 however, a slight shifting of the divide was seen when accounting for the effect of spatially
651 varied solar radiation. This is due to the fact that aspect drives vegetation differences that lead
652 to topographic asymmetry across the domain. A noticeable amount of shifting in the divide
653 was observed in the case of elevation controlled precipitation with spatially varied solar
654 radiation. Among all of the simulations, the highest divide migration was observed for the
655 orographic precipitation combined with spatially varied solar radiation. This is because the
656 slopes of the windward side of the mountain flank are gentler than the leeward slopes of the
657 mountain flank that leads to highest divide migration. Further, it was found that the divide
658 migration in the vegetated landscapes was consistent with that obtained for bare soil
659 landscapes. This suggests that the effect of vegetation protection on erosion on the windward
660 side is not as important as the erosive power of increasing runoff under orographic precipitation
661 conditions.

662 The key contribution of this modelling study is the advancement in knowledge of the
663 distribution of the vegetation cover fraction on the windward and leeward sides of the domain
664 under the influence of orographic precipitation in semi-arid ecosystems. This modelling study
665 finds that spatially varied solar radiation and non-uniform precipitation plays a fundamental
666 role in the generation of topographic asymmetry in semi-arid ecosystems.

667 **Acknowledgments**

668 This research was funded by the Australian Research Council through grants FT140100610

669 and DP140104178 (P.M. Saco) and the Scientific and Technological Research Council of

670 Turkey (TUBITAK) through grant 118C329 (O. Yetemen).

671 **References**

672 Anders, A.M., Ne, A., Roe, G.H., Montgomery, D.R., 2008. Influence of precipitation phase
673 on the form of mountain ranges. Geology (6), 479–482.
674 Anders, A.M., Roe, G.H., Durran, D.R., Minder, J.R., 2006. Small-scale spatial gradients in
675 climatological precipitation on the Olympic peninsula. Journal of Hydrometeorology 8,
676 1068–1081.
677 Arora, V.K., 2003. Simulating energy and carbon fluxes over winter wheat using coupled land
678 surface and terrestrial ecosystem models. Agricultural and Forest Meteorology 118 (1–2),
679 21–47.
680 Bass, B., Cardenas, M.B., Befus, K.M., 2017. Seasonal shifts in soil moisture throughout a
681 semiarid hillslope ecotone during drought: A geoelectrical view. Vadose Zone Journal 16
682 (2), 1-17.
683 Broza, M., Poliakov, D., Gruia, M., Bretfeld, G. 2004. Soil collembolan communities on north-
684 and south-facing slopes of an eastern Mediterranean valley. Pedobiologia, 48(5–6), 537–
685 543.
686 Carbone, R.E., Tuttle, J.D., Cooper, W.A., Grubišić, V., Lee, W. C., 1998. Trade wind rainfall
687 near the windward coast of Hawaii. Monthly weather review 126 (11), 2847–2863.
688 Carson, M.A., Kirkby, M.J., 1972. Hillslope form and process. Cambridge University Press:
689 Cambridge.
690 Caylor, K. K., Scanlon, T. M., Rodriguez-Iturbe, I. 2004. Feasible optimality of vegetation
691 patterns in river basins. Geophysical Research Letters, 31, L13502.
692 Chaboureau, J.-P., 2008. A midlatitude precipitating cloud database validated with satellite
693 observations. Journal of Applied Meteorology and Climatology 47, 1337–1353.

694 Chen, Z.S., Hsieh, C.F., Jiang, F.Y., Hsieh, T.H., Sun, I.F., 1997. Relations of soil properties
695 to topography and vegetation in a subtropical rain forest in southern Taiwan. Plant
696 Ecology 132 (2), 229–241.
697 Clift, P.D., Hodges, K.I.P.V, Heslop, D., Hannigan, R., Long, H.V.A.N., Calves, G., 2008.
698 Correlation of Himalayan exhumation rates and Asian monsoon intensity. Nature
699 Geoscience 17, 875–880.
700 Colberg, J.S., Anders, A.M., 2014. Geomorphology numerical modelling of spatially-variable
701 precipitation and passive margin escarpment evolution. Geomorphology 207, 203–212.
702 Collins, D. B. G., R. L. Bras, and G. E. Tucker (2004), Modeling the effects of vegetation-
703 erosion coupling on landscape evolution, Journal of Geophysical Research Earth Surface,
704 109, F03004
705 Collins, D.B.G., Bras, R.L., 2008. Climatic control of sediment yield in dry lands following
706 climate and land cover change. Water Resour. Res. 44 (June), 1–8.
707 Collins, D.B.G., Bras, R.L., 2010. Climatic and ecological controls of equilibrium drainage
708 density, relief, and channel concavity in dry lands. Water Resour. Res. 46 (4), 1–18.
709 Dettinger, M., Redmond, K., Cayan, D., 2004. Winter orographic precipitation ratios in the
710 Sierra Nevada - Large-scale atmospheric circulations and hydrologic consequences.
711 Journal of Hydrometeorology 5(6), 1102–1116.
712 Dietrich, W.E., Perron, J.T., 2006. The search for a topographic signature of life. Nature
713 439(7075), 411-418.
714 Eagleson, P., 1978. Introduction to water balance dynamics. Water Resour. Res. 14 (5), 705–
715 712.
716 Elder, K., Dozier, J., Michaelsen, J., 1991. Snow accumulation and distribution in an Alpine
717 Watershed. Water Resour. Res. 27 (7), 1541–1552.

718 Farquhar, G.D., Ehleringer, J.R., Hubick, K.T., 1989. Carbon isotope discrimination and
719 photosynthesis. Annual Review of Plant Physiology and Plant Molecular Biology 40,
720 503–537.
721 Ferrier, K.L., Huppert, K.L., Perron, J.T., N.D., 2013. Climatic control of bedrock river
722 incision. Nature, 1–6.
723 Garreaud, R., Falvey, M., Montecinos, A., 2016. Orographic precipitation in coastal southern
724 Chile: Mean distribution, temporal variability, and linear contribution. Journal of
725 Hydrometeorology 17, 1185–1202.
726 Gasparini, N.M., Bras, R.L., Tucker, G.E., Rice, S.P., Roy, A.G., Rhoads, B.L., 2008.
727 Numerical predictions of the sensitivity of grain size and channel slope to an increase in
728 precipitation. River confluences, tributaries and the fluvial network. John Wiley & Sons
729 Ltd., New York, NY. 367–394.
730 Gasparini, N.M., Whipple, K.X., 2014. Diagnosing climatic and tectonic controls on
731 topography: Eastern flank of the northern Bolivian Andes. Lithosphere 6 (4), 230–250.
732 Giambelluca, T.W., DeLay, J.K., Nullet, M.A., Scholl, M.A., Gingerich, S.B., 2011. Canopy
733 water balance of windward and leeward Hawaiian cloud forests on Haleakalā, Maui,
734 Hawai'i. Hydrological Processes 25 (3), 438–447.
735 Girotto, M., Cortés, G., Margulis, S.A., Durand, M., 2014. Examining spatial and temporal
736 variability in snow water equivalent using a 27-year reanalysis: Kern River watershed,
737 Sierra Nevada. Water Resour. Res. 50 (8), 6713–6734.
738 Goren, L., Willett, S.D., Braun, J., 2014. Coupled numerical – Analytical approach to
739 landscape evolution modelling. Earth Surface Processes and Landforms 545 (January),
740 522–545.
741 Guan, H., Wilson, J.L., Makhnin, O., 2005. Geostatistical mapping of mountain precipitation
742 incorporating auto searched effects. Journal of Hydrometeorology 6(6), 1018–1031.

743 Gutiérrez-Jurado, H.A., Vivoni, E.R., Cikoski, C., Harrison, B.J., Bras, R.L., Istanbulluoglu,
744 E., 2013. On the observed ecohydrologic dynamics of a semi-arid basin with aspect-
745 delimited ecosystems. Water Resour. Res. 49 (12), 8263–8284.
746 Gutiérrez-Jurado, H.A., Vivoni, E.R., Istanbulluoglu, E., Bras, R.L., 2007. Ecohydrological
747 response to a geomorphically significant flood event in a semi-arid catchment with
748 contrasting ecosystems. Geophysical Research Letters 34 (24), 1–7.
749 Han, J., Gasparini, N.M., Johnson, J.P.L., 2015. Measuring the imprint of orographic rainfall
750 gradients on the morphology of steady-state numerical fluvial landscapes. Earth Surface
751 Processes and Landforms 1350 (March), 1334–1350.
752 Han, J., Gasparini, N.M., Johnson, J.P.L., Murphy, B.P., 2014. Modeling the influence of
753 rainfall gradients on discharge, bedrock erodibility, and river profile evolution, with
754 application to the Big Island, Hawai'i. Journal of Geophysical Research: Earth Surface,
755 119(6), 1418-1440.
756 Hanson, C.L., 2001. Long-term climate database, Reynolds Creek Experimental Watershed,
757 Idaho, United States. Water Resour. Res. 37 (11), 2839–2841.
758 Hay, L.E., McCabe, G.J., 1998. Verification of the Rhea-Orographic-Precipitation Model.
759 Journal of the American Water Resources Association 34 (1), 103–112.
760 Hinckley, E. L. S., Ebel, B. A., Barnes, R. T., Anderson, R. S., Williams, M. W., Anderson, S.
761 P. (2014). Aspect control of water movement on hillslopes near the rain-snow transition
762 of the Colorado Front Range. Hydrological Processes, 28(1), 74–85.
763 Houston, J., Hartley, A.J., 2003. The Central Andean west-slope rainshadow and its potential
764 contribution to the origin of hyper-aridity in the Atacama Desert. International Journal of
765 Climatology: A Journal of the Royal Meteorological Society, 23(12), 1453-1464.
766 Houze Jr., R.A., 2012. Orographic effects on precipitating clouds. Reviews of Geophysics 50
767 (2012), 1–47.

768 Istanbulluoglu, E., Bras, R.L., 2005. Vegetation-modulated landscape evolution: Effects of
769 vegetation on landscape processes, drainage density, and topography. Journal of
770 Geophysical Research Earth Surface 110, 1–19.
771 Istanbulluoglu, E., Tarboton, D.G., Pack, R.T., Luce, C., 2002. A probabilistic approach for
772 channel initiation. Water Resour. Res. 38 (12), 1325.
773 Istanbulluoglu, E., Wang, T., Wedin, D.A., 2012. Evaluation of ecohydrologic model
774 parsimony at local and regional scales in a semi-arid grassland ecosystem. Ecohydrology
775 5 (1), 121–142.
776 Istanbulluoglu, E., Yetemen, O., Vivoni, E.R., Gutie, H.A., Bras, R.L., 2008. Eco-geomorphic
777 implications of hillslope aspect: Inferences from analysis of landscape morphology in
778 Central New Mexico. Geophysical Research Letters 35 (2), 1–6.
779 Kirchner, P.B., Bales, R.C., Molotch, N.P., Flanagan, J., Guo, Q., 2014. LiDAR measurement
780 of seasonal snow accumulation along an elevation gradient in the southern Sierra Nevada,
781 California. Hydrology and Earth System Sciences 18 (10), 4261–4275.
782 Kirshbaum, D.J., Smith, R.B., 2008. Temperature and moist-stability effects on midlatitude
783 orographic precipitation. Quarterly Journal of the Royal Meteorological Society 1199
784 (July), 1183–1199.
785 Knowles, J.F., Harpold, A.A., Cowie, R., Zeliff, M., Barnard, H.R., Burns, S.P., et al., 2015.
786 The relative contributions of alpine and subalpine ecosystems to the water balance of a
787 mountainous, headwater catchment. Hydrological Processes 29 (22), 4794–4808.
788 Kumari, N., Yetemen, O., Srivastava, A., Rodriguez, J.F., and Saco, P.M., 2019. The spatio-
789 temporal NDVI analysis for two different Australian catchments. 23rd International
790 Congress on Modelling and Simulation (MODSIM2019), Canberra, Australia, 958-964.
791 Kumari, N., Saco, P. M., Rodriguez, J. F., Johnstone, S. A., Srivastava, A., Chun, K. P.,
792 Yetemen, O., 2020. The grass is not always greener on the other side: Seasonal reversal

of vegetation greenness in aspect-driven semi-arid ecosystems. Geophysical Research Letters 47(15), e2020GL088918.

Langbein, W.B., Schumm, S., 1958. Yield of sediment in relation to mean annual precipitation. Transactions, American Geophysical Union 39.

Laursen, E.M., 1958. The total sediment load of streams. J. Hydraul. Div. Am. Soc. Civ. Eng. 84 (1530), 1–6.

Lee, T.J., 1992. The impact of vegetation on the atmospheric boundary layer and convective storms, doctoral thesis, Colorado State University, Fort Collins, Colorado.

Luce, C.H., Abatzoglou, J.T., Holden, Z.A., 2013. The missing mountain water: Slower. Science 342 (December), 1360–1365.

Lundquist, J.D., Minder, J.R., Neiman, P.J., Sukovich, E., 2010. Relationships between barrier jet heights, orographic precipitation gradients, and streamflow in the Northern Sierra Nevada. Journal of Hydrometeorology 11 (5), 1141–1156.

McMahon, D.R., 1998. Soil, landscape and vegetation interactions in small semi-arid drainage basin: Sevilleta National Wildlife Refuge, New Mexico, Nmtech, Socorro, N.M.

Meyer-Peter, E., Müller, R., 1948. Formulas for bed-load transport. In IAHSR 2nd meeting, Stockholm, appendix 2. IAHR.

Minder, J.R., Mote, P.W., Lundquist, J.D., 2010. Surface temperature lapse rates over complex terrain: Lessons from the cascade mountains. Journal of Geophysical Research Atmospheres 115, 1–13.

Moglen, G.E., Parsons, R.M., 1998. On the sensitivity of drainage density to climate change. Water Resour. Res. 34 (4), 855–862.

Montaldo, N., Rondena, R., Albertson, J.D., Mancini, M., 2005. Parsimonious modelling of vegetation dynamics for ecohydrologic studies of water-limited ecosystems. Water Resour. Res. 41 (10), 1–16.

818 Murata, F., Hayashi, Æ.T., Matsumoto, Æ.J., 2007. Rainfall on the Meghalaya Plateau in
819 Northeastern India—one of the rainiest places in the world. Natural Hazards 391–399.
820 Nearing, M.A., Simanton, J.R., Norton, L.D., Bulygin, S.J., Stone, J., 1999. Soil erosion by
821 surface water flow on a stony, semi-arid hillslope. Earth Surface Processes and Landforms
822 24 (8), 677–686.
823 Nearing, M.A., Unkrich, C.L., Goodrich, D.C., Nichols, M.H., Keefer, T.O., 2015. Temporal
824 and elevation trends in rainfall erosivity on a 149 km2 watershed in a semi-arid region of
825 the American Southwest. International Soil and Water Conservation Research 3 (2), 77–
826 85.
827 Osborn, H.B., 1984. Estimating precipitation in mountainous regions. J. Hydraul. Eng. 110
828 (12), 1859–1863.
829 Paik, K., Kim, W. 2020. Simulating the evolution of the topography-climate coupled system.
830 Hydrol. Earth Syst. Sci. Discuss. 1-24 (in review).
831 Roe, G.H., 2005. Orographic precipitation. Annu. Rev. Earth Planet. Sci. 33, 645–671.
832 Roe, G.H., Montgomery, D.R., 2002. Steady-state river profiles. Geology (2), 143–146.
833 Roe, G.H., Montgomery, D.R., Hallet, B., 2003. Orographic precipitation and the relief of
834 mountain ranges. Journal of Geophysical Research Solid Earth 108 (B6).
835 Roering, J.J., Kirchner, J.W., Dietrich, W.E., 1999. Evidence for nonlinear, diffusive sediment
836 transport on hillslopes and implications for landscape morphology. Water Resour. Res.
837 35 (3), 853–870,
838 Roering, J.J., Schmidt, K.M., Stock, J.D., Dietrich, W.E., Montgomery, D.R., 2003. Shallow
839 landsliding, root reinforcement, and the range. Canadian Geotechnical Journal 253, 237–
840 253.

841 Rozas, V., Pérez-de-Lis, G., García-González, I., Arévalo, J.R., 2011. Contrasting effects of
842 wildfire and climate on radial growth of Pinus canariensis on windward and leeward
843 slopes on Tenerife, Canary Islands. Trees - Structure and Function 25 (5), 895–905.
844 Saco, P.M., Willgoose, G.R., Hancock, G.R., Saco, P.M., Willgoose, G.R., 2007. Eco-
845 geomorphology of banded vegetation patterns in arid and semi-arid regions. Hydrology
846 and Earth System Sciences Discussions 11, 1717–1730.
847 Scaff, L., Rutllant, J. A., Rahn, D., Gascoin, S., Rondanelli, R. (2017). Meteorological
848 interpretation of orographic precipitation gradients along an Andes west slope basin at 30°
849 S (Elqui Valley, Chile). Journal of Hydrometeorology, 18(3), 713-727.
850 Shi, X., Durran, D.R., 2015. Estimating the response of extreme precipitation over midlatitude
851 mountains to global warming. Journal of Climate 28, 4246–4262.
852 Smith, R.B., 2003. A linear upslope-time-delay model for orographic precipitation. Journal of
853 Hydrology 282 (1–4), 2–9.
854 Smith, R.B., Barstad, I., 2004. A linear theory of orographic precipitation. Journal of the
855 Atmospheric Sciences 61 (12), 1377–1391.
856 Smith, T., Bookhagen, B. 2021. Climatic and biotic controls on topographic asymmetry at the
857 global scale. Journal of Geophysical Research: Earth Surface, e2020JF005692.
858 Srivastava, A., Yetemen, O., Kumari, N., Saco, P.M., 2019. Aspect-controlled spatial and
859 temporal soil moisture patterns across three different latitudes. 23rd International
860 Congress on Modelling and Simulation - Supporting Evidence-Based Decision Making:
861 The Role of Modelling and Simulation, MODSIM 2019 (December), 979–985.
862 Srivastava, A., Saco, P.M., Rodriguez, J.F., Kumari, N., Chun K.P., Yetemen, O., 2021. The
863 role of landscape morphology on soil moisture variability in semi-arid ecosystems.
864 Hydrological Processes, 35:e13990

865 Summerfield, M.A., Hulton, N., 1994. Natural controls of fluvial denudation rates in major
866 world drainage basins. Journal of Geophysical Research Solid Earth 99, 871–883.
867 Swenson, J.J., Waring, R.H., 2006. Modelled photosynthesis predicts woody plant richness at
868 three geographic scales across the north-western United States. Global Ecol. Biogeogr. 15
869 (5), 470–485
870 Thiede, R.C., Bookhagen, B., Arrowsmith, J.R., Sobel, E.R., Strecker, M.R., 2004. Climatic
871 control on rapid exhumation along the Southern Himalayan Front. Earth and Planetary
872 Science Letters 222 (3–4), 791–806.
873 Tucker, G.E., Parsons, R.M., Slingerland, R., 1997. Drainage basin responses to climate
874 change. Water Resour. Res. 33 (8), 2031–2047.
875 Tucker, G., Lancaster, S., Gasparini, N., Bras, R., 2001. The Channel-Hillslope Integrated
876 Landscape Development Model (CHILD). Boston, MA: Springer.
877 Viviroli, D., Du, H.H., Messerli, B., Meybeck, M., Weingartner, R., 2007. Mountains of the
878 world, water towers for humanity: Typology, mapping, and global significance. Water
879 Resour. Res. 43, 1–13.
880 Wainwright, J., 2005. Climate and climatological variations in the Jornada Experimental Range
881 and neighbouring areas of the US Southwest. Adv. Environ. Monit. Model. 2, 39–110
882 Whipple, K.X., Kirby, E., Brocklehurst, S.H., 1999. Geomorphic limits to climate-induced
883 increases in topographic relief. Nature 401(6748), 39–43.
884 Willgoose, G.R., 2018. Principles of soilscape and landscape evolution. Cambridge University
885 Press, Cambridge.
886 Winstral, A., Marks, D., Gurney, R., 2013. Simulating wind-affected snow accumulations at
887 catchment to basin scales. Advances in Water Resources 55, 64–79.

888 Wratt, D.S., Ridley, R.N., Sinclair, M.R., Larsen, H., Thompson, S.M., Austin, R.H.G.L., et
889 al., 1995. The New Zealand Southern Alps Experiment. Bull. Amer. Meteor. Soc. 77,
890 683–692.
891 Yetemen, O., Istanbulluoglu, E., Flores-Cervantes, J.H., Vivoni, E.R., Bras, R.L., 2015a.
892 Ecohydrologic role of solar radiation on landscape evolution. Water Resources Research
893 51 (2), 1127–1157.
894 Yetemen, O., Istanbulluoglu, E., Duvall, A.R., 2015b. Solar radiation as a global driver of
895 hillslope asymmetry: Insights from an ecogeomorphic landscape evolution model. Water
896 Resour. Res. 51 (12), 9843–9861.
897 Yetemen, O., Saco, P.M., Istanbulluoglu, E., 2019. Ecohydrology controls the geomorphic
898 response to climate change geophysical research letters. Geophysical Research Letters
899 8852–8861.
900 Zavala, V., Carretier, S., Bonnet, S., 2020. Influence of orographic precipitation on the
901 topographic and erosional evolution of mountain ranges. Basin Research (February), 1–
902 26.
903 Zou, C.B., Barron-Gafford, G.A., Breshears, D.D., 2007. Effects of topography and woody
904 plant canopy cover on near-ground solar radiation: Relevant energy inputs for
905 ecohydrology and hydropedology. Geophysical Research Letters 34 (24), 1–6.